International Journal of Multiphase Flow 201 (2026) 105753

Contents lists available at ScienceDirect

International Journal of Multiphase Flow

journal homepage: www.elsevier.com/locate/ijmulflow

Research Paper

Cavitation dynamics in the flow control section for continuous casting of steel

Willian Hogendoorn [a],*, René Delfos [a], Guus Tulen [a], Dennis Kappert [a], Stijn de Bruin [a], Job van Essen [a], Dirk van der Plas [b]

[a] Department of Process&Energy (ME), Delft university of Technology, Leeghwaterstraat 39, Delft, 2628 CB, The Netherlands
[b] Tata Steel Nederland, IJmuiden, The Netherlands

ARTICLE INFO

Keywords:
Cavitation
Continuous steel casting
Industrial flow
Shadowgraph imaging
2D water model

ABSTRACT

We investigated the flow and bubble dynamics in a stopper control valve as used in continuous casting of steel under flow conditions where cavitation or quick degassing is expected to occur. We compare the flow of a typical control stopper with four archetypical stoppers. The effect of stopper geometry on cavitation dynamics is studied experimentally in a downscaled two-dimensional water model. High-speed imaging in combination with pressure data sheds light on the performance of the various stopper geometries under cavitating and non-cavitating conditions. It is found that a blunt-ended stopper shape induces, under all conditions, a strong flow separation leading to a large pressure loss coefficient, K. In return we find that the controllability of the flow improves while K changes only marginally when entering a cavitating flow regime. In contrast, more streamlined stoppers show a lower K that yet sharply increases at the onset of cavitation; possibly causing instability in valve throughput.

1. Introduction

Continuous casting is an important process for the production of high-quality steel, since the vast majority of steel worldwide is produced using this process (Dauby, 2012; Chaudhary et al., 2011). From 1960 onwards, this method has been the dominant production process for steel casting because of the improved steel quality, energy savings, and higher product yield with respect to ingot casting. During the continuous casting process a controlled flow of liquid steel is required to enter the casting mould. To achieve this, steel is batch-wise supplied from steel ladles to a tundish. From this tundish, steel is continuously fed to the casting mould via the upper tundish nozzle (UTN) and the submerged entry nozzle (SEN). To maintain a constant level in the mould, the steel supply system features a flow control valve. Various designs of that valve exist; here we study a design that is based on a stopper that can move vertically up and down into the valve seat, Fig. 1 (Guthrie and Isac, 2022; Louhenkilpi, 2024).

Given the harsh conditions in the caster, many studies are performed using modeling approaches or numerical simulations (Thomas, 2018). Additionally, experimental studies are performed using water models given the very similar kinematic viscosity of water and liquid steel (Zhang et al., 2007; Siddiqui and Jha, 2015). As an alternative, model experiments are performed with low melting point liquid metals to mimic casting conditions (Timmel et al., 2014). The flow dynamics of liquid steel in the tundish, UTN, SEN, and the casting mould has an important effect on the final steel quality (Liu et al., 2014). This is exemplified by the variety of experimental and numerical studies focusing on these flow dynamics (Thomas, 2018). Studies include incoming unsteady turbulent flow from the SEN into the liquid pool and the effect of flow conditions on the entrainment of liquid slag from the steel surface, the transport of inclusions and gas bubbles in the mould, and their entrapment in the solidifying steel shell (Yuan et al., 2004a,b). Other studies perform surface level measurement of the molten steel in the casting mould and study the effect of the stopper-rod movement on the transient flow in the SEN and casting mould. A constant mould level is essential for a good quality of the cast product (Liu et al., 2014; Thumfart and Javurek, 2015). To control the flow of liquid steel into the mould, either stoppers or slide gate valves are employed. One study investigated the effect of a slide gate valve on the turbulent flow dynamics is studied. This study included the orientation of this slide-gate valve on the flow patterns and jet characteristics exiting the nozzle port (Bai and Thomas, 2001a,b). Chaudhary et al. (2011) studied the effect of stopper misalignment on the flow dynamics in the SEN and casting mould. Stopper misalignment is found to cause asymmetric flow in the SEN, which results in larger vortex formations and asymmetric casting mould surface velocities. To reduce residual steel in a two strand tundish, the suppression of vortex formation is studied using a rotating stopper-rod geometry. This was found to improve the yield of the steel casting process up to 2 tons per batch (Fang et al., 2024).

* Corresponding author.
E-mail address: w.j.hogendoorn@tudelft.nl (W. Hogendoorn).

https://doi.org/10.1016/j.ijmultiphaseflow.2026.105753
Received 15 September 2025; Received in revised form 9 April 2026; Accepted 29 April 2026
Available online 5 May 2026

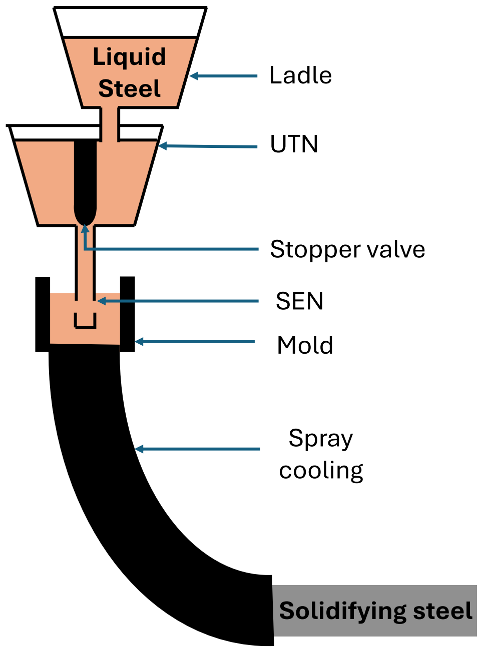

Fig. 1. An overview of the continuous steel casting process using a stopper valve.

Various non-invasive electromagnetic detection techniques have been proposed to measure the flow under the harsh conditions of continuous casting. Using mutual induction tomography (MIT) transitions in the gas/liquid flow pattern in the SEN of an industrial caster could be detected (van Oord et al., 2007) and further development of this technique has been proposed (Wondrak et al., 2014). Contactless inductive flow tomography (CIFT) was used to visualize flow patterns in a small scale liquid metal model at room temperature (Wondrak et al., 2014). These authors envision the application of CIFT in a real industrial caster using an AC-based device.

In contrast to the variety of studies on the flow dynamics and temperature distributions in the tundish and casting mould, little research focuses on the stopper shape and the effect thereof on the flow dynamics of the steel in the UTN and SEN. This is in particular relevant because the pressure decreases dramatically in the UTN when a vertical stopper-rod flow control configuration is used. Due to the high local velocity at the location of the control gap, the high density of liquid steel, and the high location in the system, the pressure is found to drop to very low values (Olia et al., 2023). There are two possible scenarios that might happen due to this low pressure: local cavitation or degassing bubbles may be formed in the liquid steel or gas aspiration might occur through the porous refractory walls. Such phenomena can result in instabilities or failure of the feeding system. Though various authors have addressed this topic (Javurek et al., 2010; Liu et al., 2014; Olia et al., 2023; Thumfart and Javurek, 2015), knowledge on the actual flow phenomena in the stopper throat is still limited. This is predominantly due to a lack of data from direct plant measurements owing to the harsh conditions during steel casting and the lack of laboratory experiments to validate the mathematical models or test these hypotheses (Javurek et al., 2010; Liu et al., 2023). This lack of insight sets the motivation for this experimental study.

Using a scaled two-dimensional water model it is shown that cavitation occurs at mass flow rates that are comparable to real-life casting conditions. The formation and presence of these cavitation bubbles creates instabilities in the mass flow rates and disrupts the continuity of the liquid steel outflow. Different stopper geometries are proposed that will enhance the controllability of the mass flow rate.

Table 1
Pressure sensor locations of the left-hand-side of the geometry. The other (symmetry) sensor locations exhibits mirror symmetry with respect to the x-axis.

Sensor	x-position (mm)	z-position (mm)
p_i	−28	−7
p_{G_1}	−22	−14
p_{G2}	−20	−22
p_o	−20	−40

The outline of this paper is as follows: the experimental procedure and data processing are provided in Section 2. The results obtained and a discussion thereof are presented in Section 3. A summary and conclusion is given in Section 4.

2. Experimental procedure

2.1. Experimental facility

A schematic overview of the experimental setup can be seen in Fig. 2. The closed-loop system consists of a reservoir with dimensions L, H, and W, which are 1.0, 0.15, and 0.48 m, respectively. The flow loop is filled with standard degassed tap water at a temperature of 20 °C. The flow is driven by a centrifugal pump (KSB ETACHROM BC 025-125.1/072) with a maximum flow rate of 250 L/min and a maximum head of 10.3 m. The flow rate is measured using an electromagnetic flowmeter (FLOWTEC Picomag DMI 6530), with a measurement range up to 60 L/min. Pressure measurements are taken symmetrically on both the left and right sides of the throat of the model. To track the pressure evolution over the stopper region, four sets of sensors are used. The inlet pressure is measured at the bottom of the reservoir, denoted as p_i. In the throat region, i.e. the narrowest part around the flow control gap, two sets of sensors are used, positioned just before and just after the narrowest section of the throat. These sensors are denoted as p_{G1} and p_{G2} in the inset in Fig. 2, where the subscript G refers to the gap location. Additionally, another set of pressure sensors, p_o, are placed downstream of the stopper geometry to measure the pressure loss over the stopper; the subscript o refers to the outlet location. The exact pressure sensor locations in mm are added in Table 1 The pressure sensors used are the Board Mount Pressure Sensor -15psi to 15psi Differential Medical 8-Pin DIP Module (type: Honeywell HSCDRNT015PDSA3). The pressure data were sampled using an Arduino Nano V3.0 (ATmega328P) with a sampling frequency of 200 Hz. Temperature measurements are taken using a thermocouple probe (type: Type K P3400 Thermocouple). Flow visualizations are obtained using high-speed imaging (PHOTRON Nova S12 Fastcam) with a resolution of 1024 × 1024 px^2, resulting in a field of view of 100 × 100 mm^2, a 105 mm AF f2.8 Nikkor object-lens in combination with LED back-illumination. The images were recorded at a frame-rate of 12800 Hz.

2.2. Experimental model and dimensional similarity

The UTN and stopper in the TATA Steel factory exhibits axis-symmetry along the vertical axis (z-direction), which we translated into a 2D left–right symmetric water model. 2D water model as well. The 2D model is scaled down by factor of 2 to ensure that cavitating conditions are achieved by the current pump. A schematic of the 2D water model design is shown in Fig. 2. The 2D stopper, top plate, and stopper geometry are constructed using PMMA, enabling optical access to the cavitation phenomena. The gap in the throat is defined as the narrowest passage between the stopper geometry and the wall and is shown in the inset in Fig. 2. D_h is the hydraulic diameter of the gap, defined as

$$\mathrm{D_h} = \frac{2wt}{w+t}, \tag{1}$$

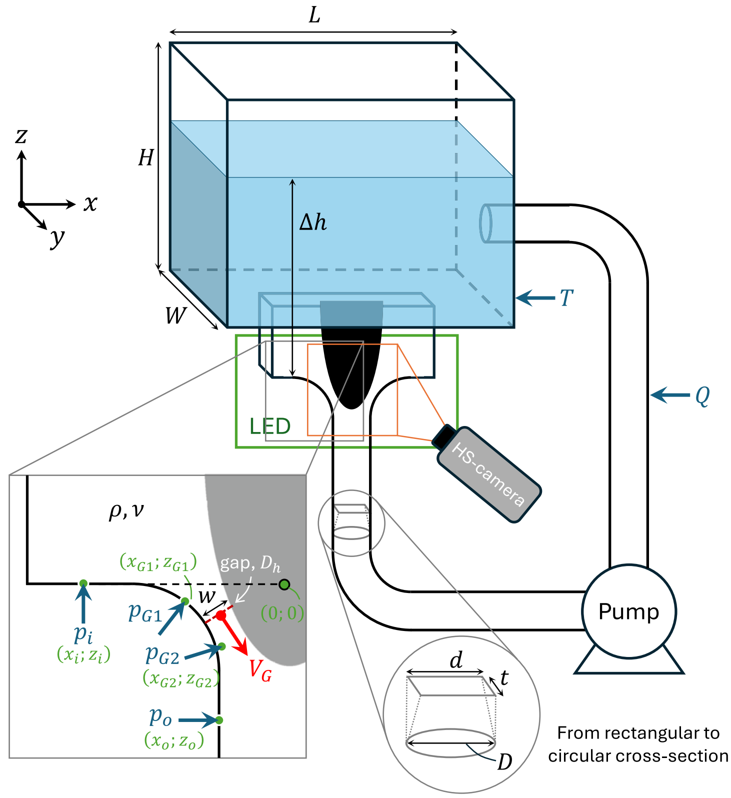

Fig. 2. Schematic of the experimental setup including the water reservoir, reference stopper geometry, pump, flow meter, temperature sensor and the high-speed camera with the corresponding LED panel that is used for the shadowgraphy measurements. The inset shows the control gap with the corresponding pressure locations.

with w and t the gap width and thickness, respectively. Thus the gap velocity, V_G, can be adjusted by increasing the height of the stopper between 4.0 and 6.0 mm, using 1.0 mm thick aluminum shims. Due to the shape of the geometry, w varies as function of the stopper height, and is found to be $w = 1.7$, 2.2, and 2.4 mm for stopper heights of 4.0, 5.0, and 6.0 mm, respectively. The thickness, t (i.e., in the y-direction) of the 2D duct is chosen as 6.0 mm; which was suitable with available means and always considerably more than w at the narrowest point, such that flow boundary layers from the geometry were predominant rather than those from the front and rear walls. The width of the downstream PMMA section is 41 mm.

To achieve similar flow conditions in the 2D water model as the flow conditions in the caster, dimensional scaling is applied. In this study three groups are relevant. In the first place the Reynolds number:

$$\mathrm{Re} = \frac{V_G D_h}{\nu}, \tag{2}$$

where V_G the average velocity at the location of the gap, and ν is the fluid kinematic viscosity. The second dimensionless group is the cavitation number, defined as

$$\sigma = \frac{2(p_G - p_v)}{\rho V_G^2}, \tag{3}$$

where p_G is the pressure at the position of the gap, and p_v the fluid vapor pressure and ρ the density of the fluid. And the last dimensionless group is the Weber number:

$$\mathrm{We} = \frac{\rho l V_G^2}{\gamma}, \tag{4}$$

where l is the characteristic length scale, and γ the surface tension. Simultaneous scaling of these three dimensionless groups is not feasible. Given the focus of the current study, dimensional similarity is achieved using σ. This implies that the Reynolds number of the 2D water model (w) is found to be reasonably close to the Reynolds number of the steel caster (s), i.e., $Re_s = Re_w \approx 10^4 - 10^5$, both thus being in the turbulent regime. The Weber number is found to differ considerably, due to the high surface tension of steel: $We_s \approx 10^3$ and $We_w \approx 10^4$. Although We_s and We_w differ by one order of magnitude, both values are within a range that lead to small cavitation bubbles (Cui et al., 2023), suggesting that this difference likely will have little influence on the results.

The cavitation number can be scaled by adjusting the hydrostatic pressure of the system or the flow velocity. In the experimental setup a centrifugal pump with frequency control was used, which allowed us to scale the cavitation number through the gap velocity, V_G.

During the experiments, it was found that the rise in water temperature throughout an experimental series was limited to 1 °C, and therefore deemed to have a negligible effect on the fluid properties.

In addition to the reference stopper, four archetypal stopper geometries are introduced, see Fig. 3. These geometries are all characterized by different, extreme expansion and contraction angles at the inlet and outlet. This results in either a very fast or smooth contraction of the flow channel between the stopper and upper part of the SEN, and allows to study the effect thereof on the flow control characteristics and cavitation dynamics. Note that the outline of the reference stopper, indicated by the red dashed line, is superimposed on the four other stopper geometries. This highlights that the shape of these stoppers in the narrowest section of the throat is the same for all these stoppers. Hence, the resulting gap width (or D_h) at a given stopper height was the same for all stoppers. This is also confirmed by comparing the gap-width from the different stopper geometries from the reference high-speed images.

The pressure loss coefficient, K, for the these geometries is given by:

$$K = \frac{2\Delta p}{\rho V_G^2}, \tag{5}$$

where Δp is the difference between the pressure at the flow entering the flow control valve, p_i, and the pressure measured downstream of

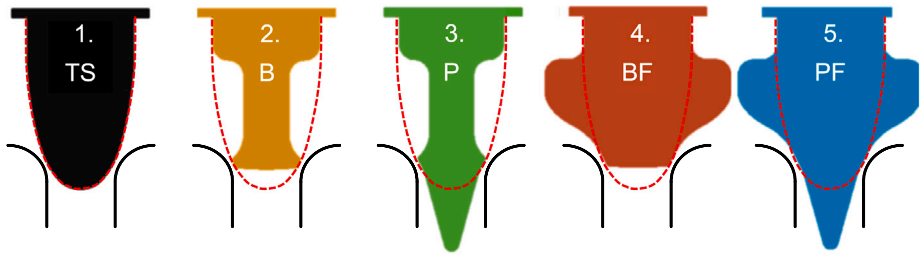

Fig. 3. An overview of the five different stopper geometries used in this study. The outline of the reference stopper (TS) is superimposed on the four other stopper geometries, to highlight that the gap-with is the same for all geometries.

the flow control valve, p_o, see the inset in Fig. 2. For p_i we have used the hydrostatic pressure at the bottom of the water reservoir, based on the water level, $\Delta h = 0.29$ m, which was kept constant throughout the experimental campaign. For the atmospheric pressure we have used a constant value of 1.01 bar.

2.3. Measurement procedure and data processing

The experiments were conducted at stopper heights of 4.0, 5.0, and 6.0 mm to investigate the effect of the operating stopper height on the flow control characteristics and cavitation phenomena. These heights were selected to study both non-cavitating and cavitating flows. Cavitation inception is found to occur for a pump drive speed between 40% and 80% of maximum 2855 RPM, depending on stopper height and geometry. Prior to each experiment, the flow loop was operated under cavitating conditions for at least 5 min to remove dissolved gases from the water and ensure consistent experimental conditions.

The measurement procedure was carried out as follows: initially, the pump was set to operate at 40% speed, and the 10-second average flow rate was documented. Then the operating frequency of the pump drive was increased by 2%, the new flow rate was documented. This incremental process continued up until a pump speed of 80%. This limit was chosen to prevent cavitation damage to the impeller of the pump. Under all flow conditions, the pressure data of the eight pressure sensors was recorded.

Additionally, for each stopper geometry and height, recordings were taken with the high-speed camera at 40% pump speed. At these flow conditions no cavitation was observed, hence from these images the gap width, w (required for D_h) is obtained. The gap width is determined using a calibrated camera image in combination with a sub-pixel fit to improve accuracy. Another recording was taken at 80% pump speed for observing cavitating flow.

To ensure accurate pressure data, a 10-second average was first calculated for each pressure sensor, followed by averaging the readings from the symmetrically positioned sensor pair at the same height.

3. Results

The shadowgraphy images for the reference stopper geometry for increasing cavitation number are shown in Fig. 4. Cavitation inception is observed for $\sigma_i = 0.40$. The location of the cavity cloud is indicated with a red arrow in Fig. 4(a). Note that cavitation starts on the left side of the stopper and is not yet observed on the right side. Even though the stopper seems symmetrically oriented in the gap, cavitation inception is very sensitive to the smallest misalignment and hence a small difference in local pressure. Furthermore, it can be observed that the bubbles form on the outer wall and not on the stopper geometry itself. This is due to the flow that separates on the side of the outer wall, i.e. the wall with the highest curvature hence the lowest static pressure. This flow separation is more obvious from the cavitation bubbles in the shadowgraph images at lower σ. For decreasing σ, cavitation bubbles are generated on both sides at the outer wall, as is shown in Fig. 4(b). The bubbles are transported downstream, where they collapse in the higher pressure region. Even more pronounced cavitation is observed for $\sigma = 0.058$, shown in Fig. 4(c). To visualize the flow patterns that are present in this image, a time-averaged image over 61 frames (i.e., corresponding to approximately 5 ms) is shown in Fig. 4(d). This image displays the 'semi-instantaneous' flow patterns, including a flow recirculation area downstream of the stopper geometry. Using 61 frames for averaging were found to give a good balance between the grayscale intensity and visibility of the semi-instantaneous flow structure. For this selected averaging window, short-time fluctuations and noise are suppressed while retaining coherent structures. It is important to note that these averaged images are intended for a qualitative illustration of the dominant flow topology rather than statistically converged flow fields. The flow dynamics can also be observed from the supplemental video (S1). Furthermore, from the location of the bubbles, the flow after the gap is found to attach to the stopper geometry, and separates on the side of the SEN.

The visualizations for the additional four stopper geometries are shown in Fig. 5. Note that these images were captured at the end of each measurement series, with the pump operating at 80% of its maximum capacity. Although there is some variation in Re (or σ), the Reynolds numbers for these flow conditions vary between $Re = 37\,000$ and 40 000, and are comparable to the Reynolds number of Fig. 4(d), with $Re = 37\,500$. On the left-hand-side the instantaneous images are shown, and on the right-hand-side the corresponding averaged image is added to highlight the flow patterns for the different stopper geometries. Again, for the averaged image, 61 frames are used, which is found to be sufficient to show 'semi-instantaneous' flow patterns. Videos illustrating the flow patterns for the different geometries are provided in the supplemental material (S2–S5).

It is interesting that for both blunt-ended stopper geometries (Fig. 5(b and d)), flow recirculation zones or vortices are observed. For both stoppers the flow is found to separate from the sharp edge on the side of the stopper as indicated with the red arrows. The flow remains attached to the wall of the SEN causing a shear layer and the resulting recirculation zone below the stopper (Idelchik et al., 1986). For the smooth-ended stoppers (3 and 5), the flow separates on the wall of the SEN (Fig. 5(f and h)), and for stopper 3 also on the sharp inlet edge of the stopper itself (Fig. 5(f)). In contrast to the blunt-ended stoppers no large-scale vortices are observed as the cross-sectional area gradually increases for these stopper geometries. This is further supported by the average pressure drop measurements discussed in the following section.

Fig. 6(a) and (b) show the pressure loss coefficient (K) as a function of the cavitation number (σ) and Reynolds number (Re), respectively, for a stopper height of 4.0 mm. Starting from high σ (i.e., low Re), all stopper geometries show a relatively constant or slight reduction of K for decreasing σ. The same behavior for K is observed for increasing Re.

This behavior continuous until cavitation inception is observed for $\sigma_i \approx 0.25$ and $Re \approx 35\,000$, depending on the stopper geometry. For lower cavitation numbers, i.e., more intense cavitation, the pressure loss coefficient is found to steeply increase. This behavior is most pronounced for the smooth-ended stopper geometries (i.e., stoppers 3 and 5).

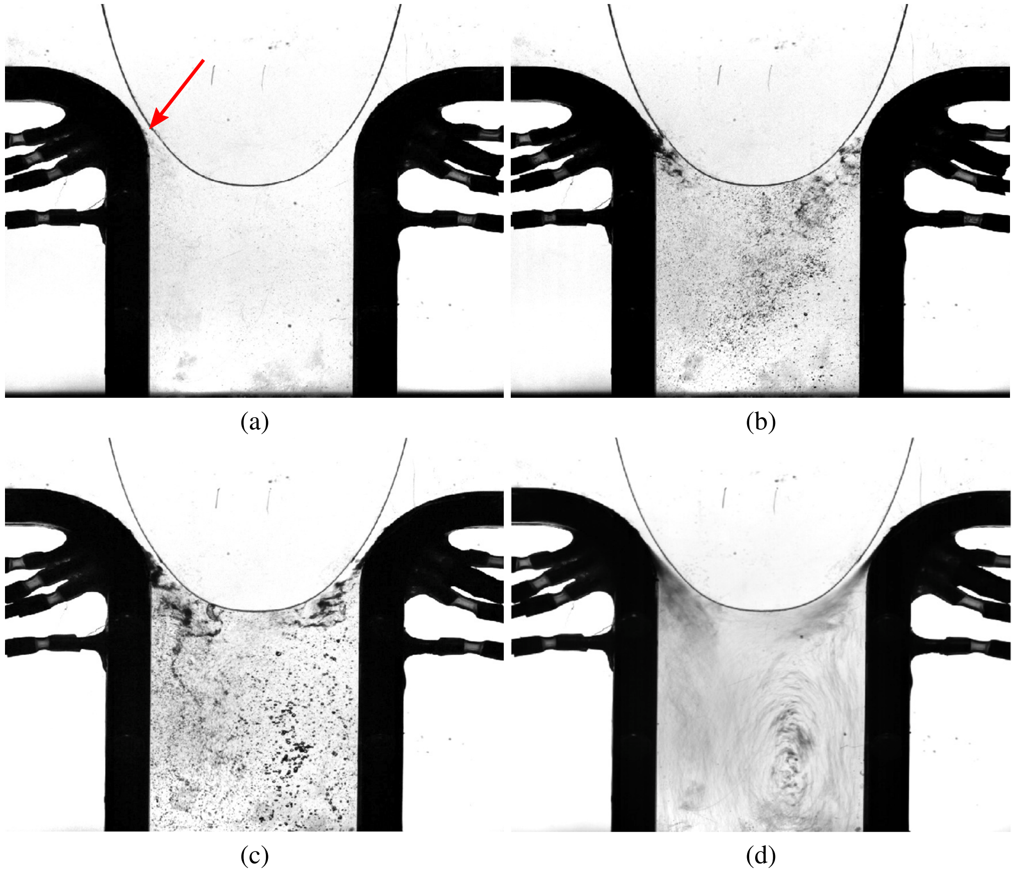

Fig. 4. Shadowgraphy images for the reference stopper geometry for increasing cavitation number for h = 4.0 mm. Cavitation inception is observed for σ = 0.40 and Re = 31 800 in (a), as indicated by the red arrow. The flow conditions in (b) and (c) correspond to σ = 0.095 and 0.058 and Re = 36 700 and 37 500, respectively. The shadowgraph image in (d) is an averaged image to visualize the flow patterns in (c). (For interpretation of the references to color in this figure legend, the reader is referred to the web version of this article.)

Note that for the stopper geometries with a sudden contraction (i.e., stoppers 2 and 3), σ is based on the pressure measured by the third sensor (p_{G2}) instead of the second sensor (p_{G1}). The p_{G1} sensor readings for both geometries were found to be affected by the flow separation from the stopper right before the gap. By using the p_{G2} sensor reading, the lowest pressure in the gap was obtained. This is also confirmed by the pressure colormaps that are discussed later on, and presented in Fig. 9. For these stoppers the lowest pressure (i.e., darkest spots) occur for the p_{G2} pressure reading. Very similar curves are obtained if σ is based on the theoretical pressure in the gap, using the hydrostatic pressure at the location of the gap in combination with the dynamic pressure, i.e., $\sigma' = (\rho g h + p_{atm} - p_v)/\frac{1}{2}\rho V_G^2 - 1$.

The curve corresponding to the reference stopper geometry falls in-between the other curves, exhibiting the intermediate behavior of this geometry. This is not surprising, given the elliptic shape of this geometry (see, Fig. 3) that results in an 'intermediate' contraction and expansion of the flow channel between the stopper and the upper part of the SEN.

Interestingly, both blunt-ended stoppers (i.e., 2 and 4) show a similar pressure loss coefficient curves, with only a minor difference for cavitating conditions. This suggests that K is mainly governed by the downstream geometry. Furthermore, these stoppers have a significantly higher K over the full range of σ or Re compared to the other geometries. Idelchik et al. (1986) reports a pressure loss coefficient of $K \approx$ 0.87-0.92 for a sudden expansion, derived using the *Borda-Carnot* equation and based on the gap and downstream cross-sectional areas. This pressure loss coefficient is of similar order of magnitude as the pressure loss coefficient we measured for both stopper geometries, $K \approx$ 0.8–1.0. The pressure losses are attributed to the flow separation at the trailing edge leading to the formation of large eddies downstream of the sudden expansion, as can also be observed in Fig. 5(b) and (d) (Idelchik et al., 1986).

For the blunt-ended stoppers we have seen that K is predominantly governed by the downstream geometry. This is further supported by comparing the plateau values for K for the different stopper geometries. To determine the upstream pressure drop contribution we can also compare stoppers 3 and 5 (in addition to stoppers 2 and 4 that are discussed above), by keeping the downstream geometry constant. This results in a difference in K of approximately 0.1. For increasing stopper height, this difference becomes even smaller. For stopper heights of 5.0 and 6.0 mm a difference in K of approximately 0.07 and 0.04 are found, respectively (see, Figs. 7 and 8). The same analysis can be done for the contribution of the downstream geometry. For this we keep the upstream geometry constant and find a difference in K of approximately 0.3 and 0.4 for stoppers 2 and 3, and 4 and 5, respectively. This is also consistent for increasing stopper heights.

No significant effects for the pressure loss coefficient curves are observed for increasing stopper heights. Increasing the height will result in a slightly higher K for all stopper geometries. When comparing the curves from Fig. 8 with Fig. 6, the pressure loss coefficient is found to increase with $K \approx 0.1$. This can be explained by a lower contraction ratio (i.e., stopper gap width vs inflow or outflow cross-sectional area), which requires a higher pressure difference needed for cavitation inception. Since the upstream pressure is kept constant throughout the experiments, this higher pressure difference is achieved by decreasing the downstream pressure through a higher pump speed resulting in a higher flow rate. This is confirmed by comparing the Reynolds numbers at which cavitation inception occurs. Re increases

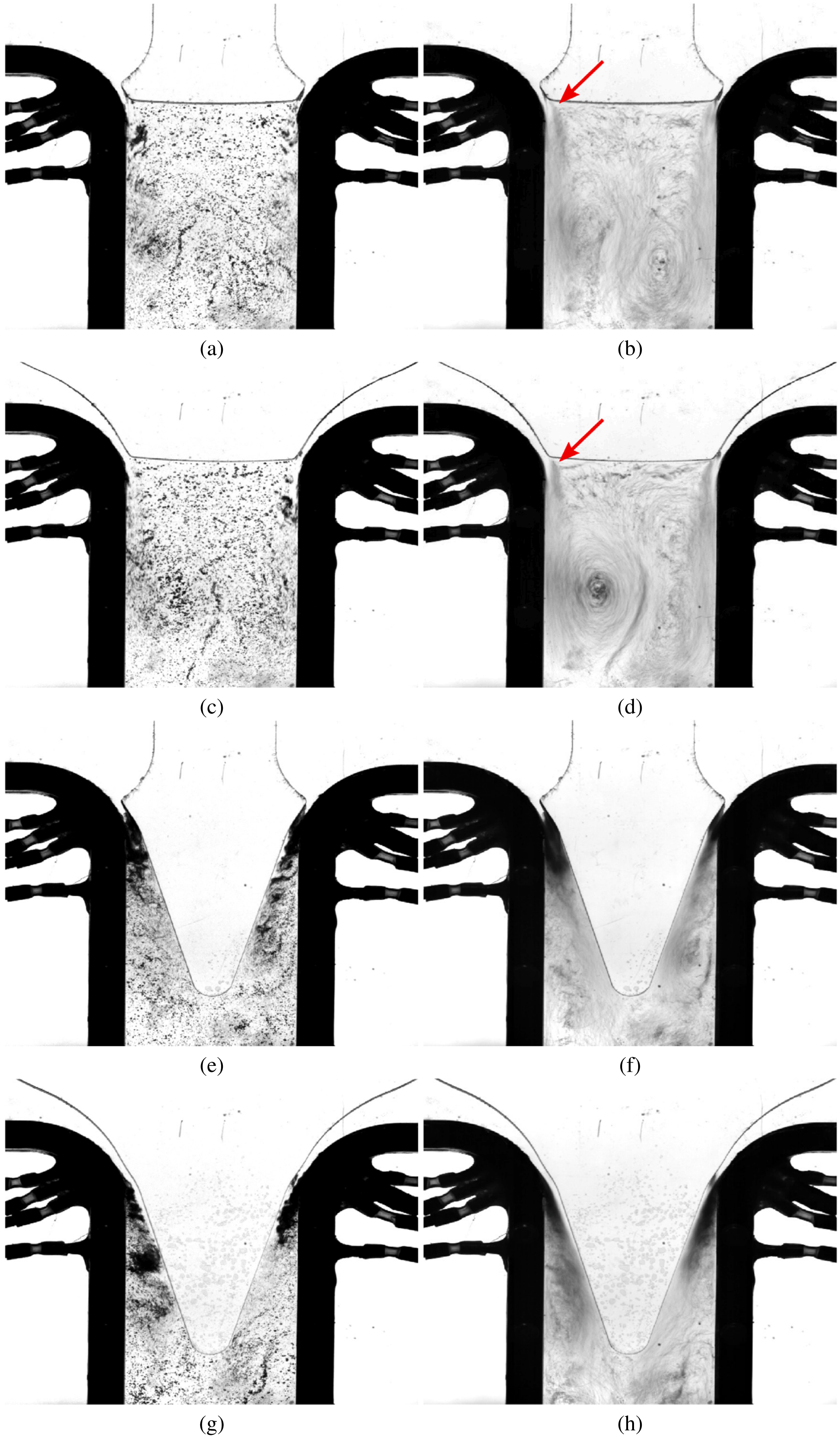

Fig. 5. Instantaneous (left) and averaged (right) shadowgraph images for the four different stopper geometries 2-5 for h = 4.0 mm. The cavitation conditions in (a), (c), (e), and (g) correspond to σ = 0.094, 0.074, 0.035, and 0.040, respectively. The Reynolds number is relatively constant, and corresponds to Re = 37 700, 38 900, 37 000, and 40 000.

from approximately 37 000 in Fig. 6 to approximately 50 000 in Fig. 8.

It is striking to observe that the hydrodynamically smooth stopper (i.e., stopper 5) has a delayed onset of cavitation, irrespective of the stopper height. This can be seen from the fact that the sharp increase in K for this stopper takes place at the highest Re. However, upon cavitation inception, this stopper exhibits a strong increase in K, for a pressure driven system resulting in a difficult flow control behavior:

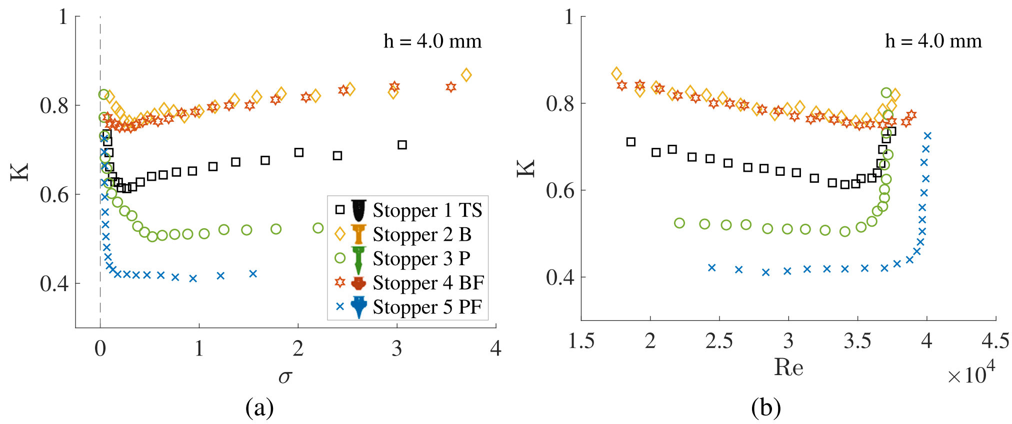

Fig. 6. (a) Pressure loss coefficients, K, as function of the cavitation number, σ and (b) K as function of the Reynolds number, Re, for a stopper height, h = 4.0 mm. The five different stopper geometries are indicated in the legend in (a).

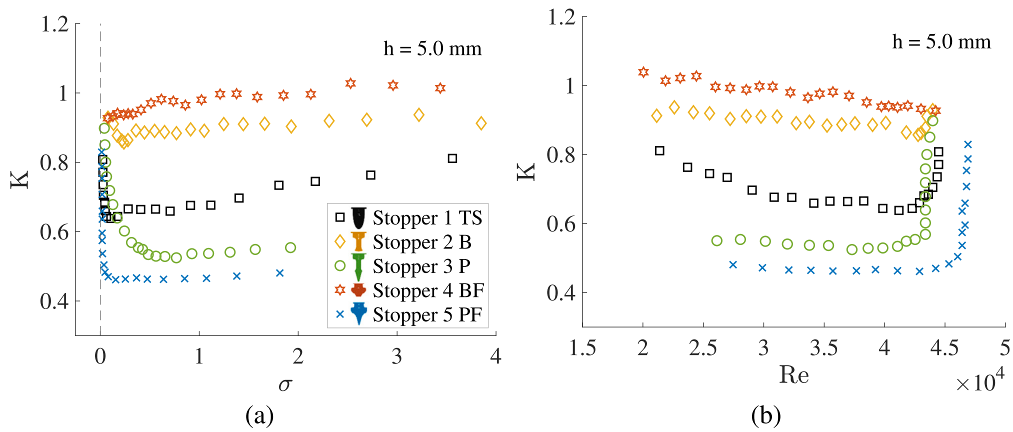

Fig. 7. (a) Pressure loss coefficients, K, as function of the cavitation number, σ and (b) K as function of the Reynolds number, Re, for a stopper height, h = 5.0 mm. The five different stopper geometries are indicated in the legend in (a).

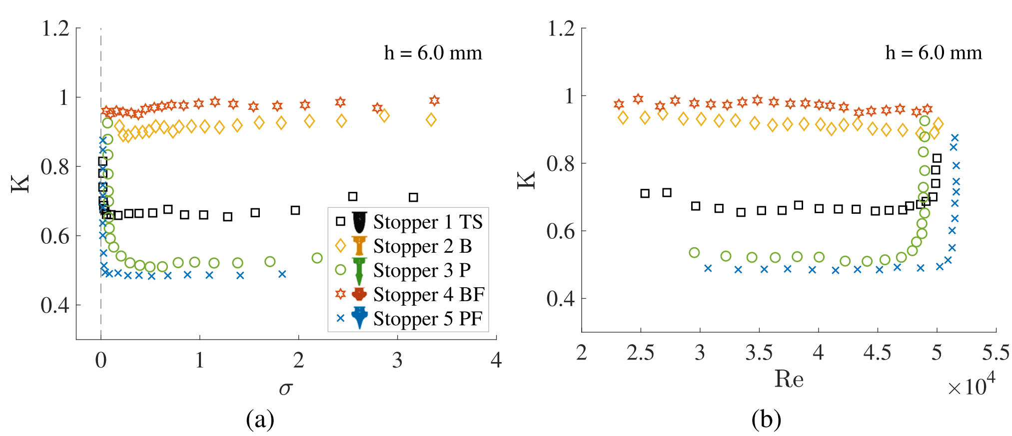

Fig. 8. (a) Pressure loss coefficients, K, as function of the cavitation number, σ and (b) K as function of the Reynolds number, Re, for a stopper height, h = 6.0 mm. The five different stopper geometries are indicated in the legend in (a).

a small increase in velocity may lead to a step-up increase in pressure loss, hence to a deceleration of the flow; as a result giving a step-down in pressure loss, then causing the flow to accelerate again. This cyclic phenomenon is more often encountered when controlling hydrodynamic systems, including pipe flows that are operated around laminar to turbulent conditions. When flows in pipes approach turbulent conditions, the emerging local turbulent patches will increase the pressure drop, which will result in re-laminarization of the flow. The step-down in pressure loss will increase the flowrate, resulting in the formation of local turbulent patches again Avila et al. (2011). In control theory this cyclic phenomenon is known as hunting, where the flow control input is in a continuous feedback loop with the measured flow output (Eames et al., 2014). The same applies, albeit to a lesser extent, to the first and third stopper. This behavior complicates the control of these stoppers within this operational area. Moreover, for a low K, a high gap velocity, V_G, is required to realize the same pressure

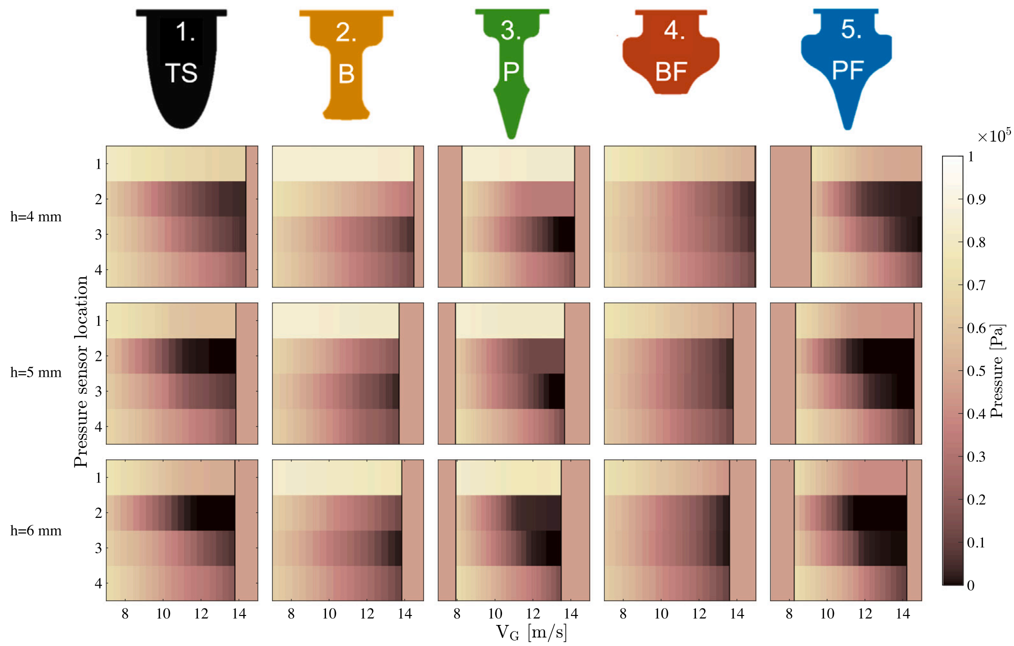

Fig. 9. Pressure colormaps for the different stopper geometries, as function of the stopper heights, h, and gap velocities, V_G. The pressure sensor locations correspond to 1: p_i, 2: p_{G1}, 3: p_{G2}, 4: p_o.

drop compared to stopper geometries with a high K. Additionally, smaller gap sizes are more vulnerable for fouling and wear, again affecting the control behavior. In contrast, the blunt-ended stoppers (i.e., 2 and 4) exhibit a relatively constant K over the full range of operation, even under cavitating conditions. The combination with a lower gap velocity makes these stoppers less vulnerable for fouling and are therefore considered ideal for better effective control over the full operational range. Provided that the upstream section of the geometry has a modest effect on K, it is anticipated that any upstream geometry that falls between the geometry of stopper 2 and stopper 4 could be used to achieve similar flow control behavior.

The pressure colormaps for the different stoppers for increasing gap velocity, V_G, are shown in Fig. 9. For each stopper three different heat maps are presented, each representing a different stopper height. The pressure sensor locations correspond to 1: p_i, 2: p_{G1}, 3: p_{G2}, and 4: p_o. It can be seen that for every case the inlet pressure, p_i is the highest, as expected by the relatively low entrance velocity. For increasing V_G this pressure is found to decrease. In general, the lowest pressures are found for both pressure sensors in the gap, p_{G1} and p_{G2}. Interestingly, for both stoppers with the hydrodynamically blunt inlets (stopper 2 and 3), the lowest pressure is measured at the location of pressure sensor p_{G2} due to upstream flow separation. Being in contrast with the other stopper geometries where the lowest pressure is measured at the location of pressure sensor p_{G1}. For stopper geometry 4, the smoothest pressure profile is observed, which is consistent with the discussion above. In contrast, for stopper geometry 5 the pressure is found to rapidly drop to cavitation conditions, as can be seen from the dark regions for both pressure sensors in the gap.

For more intense cavitation conditions, $\sigma \approx 0.02$, the formation of condensation waves (also referred to as condensation or bubbly shocks) is anticipated (Ganesh et al., 2016; Jahangir et al., 2018; Gawandalkar and Poelma, 2024). Even though these cavitation conditions are not likely to occur during standard operation conditions in the caster, it is intriguing that these phenomena known from idealized flow studies are observed in an area with practical industrial application as well. The location and propagation of the condensation wave front are indicated by the yellow arrows in Fig. 10. Initially, it can be seen that the wave is formed from another cavity cloud that collapsed (Fig. 10(a)). Subsequently, this wave front travels upstream through the growing cavity on the right (Fig. 10(b–g)), eventually reaching the throat (Fig. 10(h)). The propagation of the condensation wave front through the cavity is also visible in the video in the supplemental material (S6). Additionally, in this video it can be seen that the condensation wave is traveling through the entire domain below the stopper, responsible for local density variations.

This observation of a condensing wave front is consistent with findings from studies on partial cavitation in idealized flow configurations, such as a two-dimensional wedge (Ganesh, 2015) and a three-dimensional axisymmetric venturi (Gawandalkar and Poelma, 2024). However, important differences limit the direct applicability of these results to the present flow configuration. In particular, the referenced studies focus on partial cavity regimes with consistent periodic shedding within idealized and well-defined geometries, whereas the current case involves a more complex flow structure and the corresponding irregular flow interactions. A more detailed interpretation is beyond the scope of this work. Specifically, a rigorous analysis based on the 1-D Rankine–Hugoniot relation, following from the mass and momentum conservation equations together with the binary mixture model for density, would require accurate time resolved information on the local pressure and void fraction upstream and downstream of the condensation wave front.

A key question in the present study is to what extent the cavitation behavior observed in a water model can be applied to cavitation in liquid metals. The current scaling approach, which is based on a Reynolds and cavitation number similarity, provides a solid basis for reproducing the dominant flow structures and onset of cavitation. The mismatch in Weber number similarity (i.e., the discrepancy in surface tension) implies that the size of the cavitation bubbles are not fully matched. However, both Weber numbers are in a range that lead to small cavitation bubbles (Cui et al., 2023). This suggests that key features of cavitation inception and large-scale flow interactions are likely to be captured with reasonable accuracy in the water model. This is further supported by the study by Lee et al. (2013), which indicates that, despite the complexity of liquid metal systems, the fundamental processes of bubble growth and collapse remain governed by a similar response to pressure field fluctuations. Similarly, Tzanakis et al. (2015) demonstrate in a comparative study between water and liquid aluminum that cavitation bubbles are generated for comparable ultrasonic

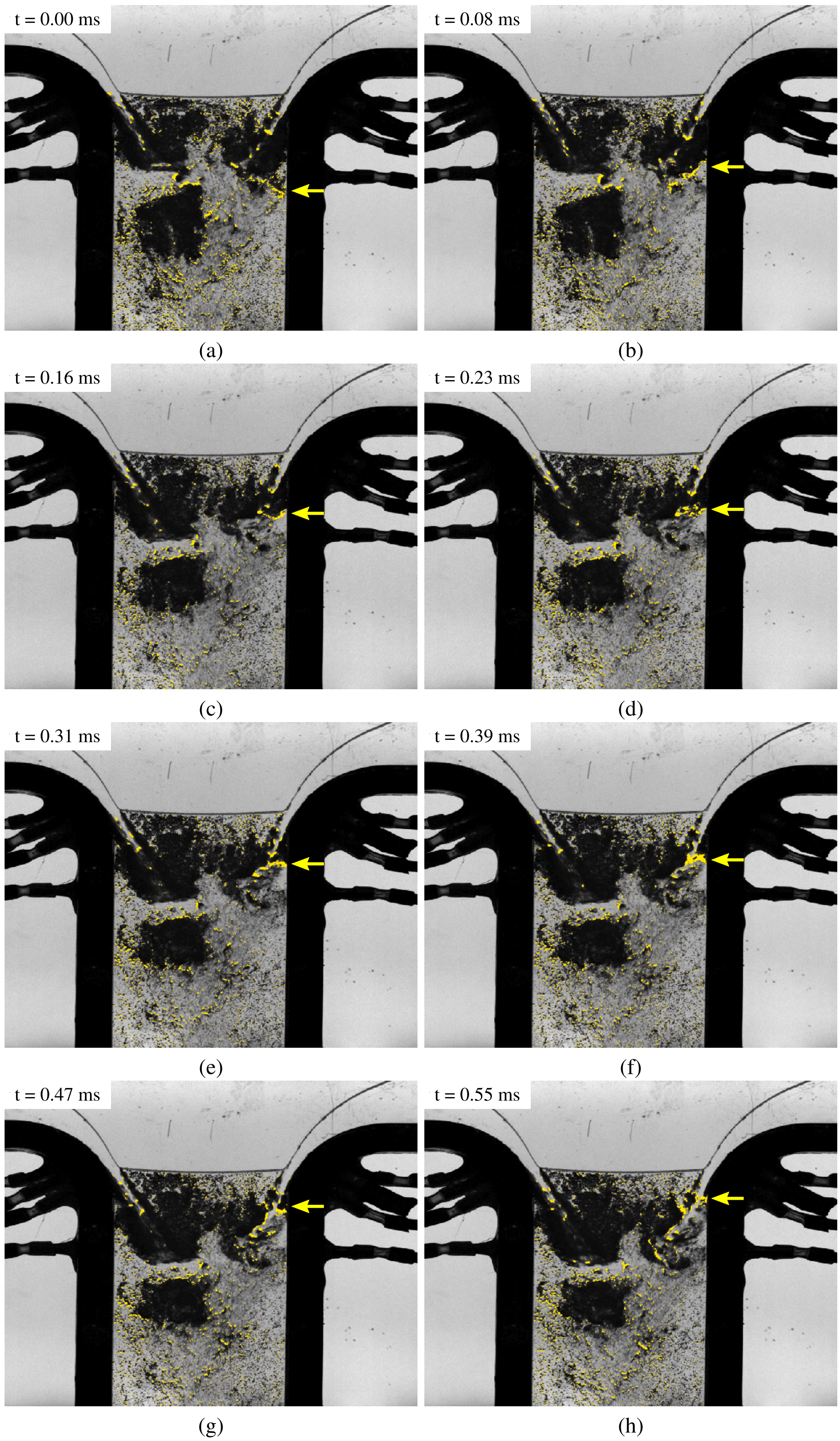

Fig. 10. Propagation of the condensation wave for the blunt-ended stopper geometry with a smooth inflow (stopper 4) for h = 6.0 mm and $\sigma \approx 0.02$. The disappearing cavities are indicated by the yellow patches using an enhanced gradient shadowgrapy approach (Gluzman and Thomas, 2022). The yellow arrows indicate the location of the condensation wave front that travels upstream through the cavity on the right. (For interpretation of the references to color in this figure legend, the reader is referred to the web version of this article.)

excitation conditions, supporting the observation that qualitative trends are similar for different fluids. However, acoustic profile measurements show one important difference, which is the much higher cavitation intensity observed in liquid aluminum compared to water. This is further supported by cavitation erosion tests in different test fluids conducted by Hattori et al. (2013). In their study the authors show that cavitation in a liquid metal alloy (i.e., a lead–bismuth) was found to be up to ten times more damaging than cavitation erosion in deionized water. This shows that for cavitating conditions, the cavitation intensity and erosion damage are more profound for liquid steel than for water. Therefore, while the current results provide valuable insight into cavitation behavior, their quantitative extrapolation to liquid steel requires careful consideration.

An additional consideration is the distinction between vaporous and gaseous cavitation and the role of nuclei content. In water, cavitation generally involves both vaporous and gaseous mechanisms, whereas in liquid metals such as steel, cavitation is expected to be predominantly gaseous. This is due the presence of dissolved gasses, notably nitrogen, hydrogen and carbon monoxide in liquid steel. For typical industrial steel grades, containing some 40 ppm of nitrogen, gaseous evaporation would start at pressures around 1000 Pa (Deo and Boom, 1993). This is at least one order of magnitude larger than the vapor pressure of iron and other metals such as Si and Mn that are present in steel. Therefore, it is important to mention that even for cavitation number similarity, the bubble dynamics, and in particular implosion, may not be directly comparable. Additionally, cavitation inception in liquids is known to be controlled by the presence of nuclei rather than by the intrinsic tensile strength of the liquid (Mørch, 2015). The use of tap water in the present study implies a relatively high nuclei density due to dissolved gases and impurities, promoting earlier cavitation inception. This is similar to liquid steel, that contains about 20 ppm of micron-size oxidic inclusions. In contrast, deionized water typically contains fewer nuclei, resulting in increased tensile strength and delayed inception, as demonstrated by Marschall et al. (2003). Therefore, it is anticipated that the results from the present study reflects the gaseous cavitation type. In gaseous cavitation, bubbles do not collapse violently but gradually dissolve, making it less erosive than vaporous cavitation. While this mitigates potential damage to the SEN or stopper, it can still induce flow blockage and instabilities, similar to the flow resistance characteristics reported in the present study.

4. Conclusion & outlook

Based on the results of this study, it is a probable scenario that cavitation occurs in flow controllers in industrial steel casters. Yet, the exact conditions depend on the casting speed and the hydraulic gap diameter, D_h. For the reference stopper geometry and a stopper height of 4.0 mm in our water model, cavitation inception is measured for $\sigma_i \approx 0.25$, and corresponds to $Re_w \approx 35\,000$. To compare, for an axi-symmetric industrial stopper and a liquid steel density of $\rho_s = 7000$ kg/m^3 and the ferrostatic pressure from the 1 m steel in the tundish, this corresponds to a typical gap velocity of approximately 5.5 m/s. Considering a typical tundish flow velocity of around 0.2 m/s, the local velocities in the valve seat – especially during high casting rates – are observed to exceed the critical gap velocity, indicating the formation of cavitation bubbles in this area (Zhong et al., 2007).

The additional stopper geometries in this study are characterized by extreme inlet and outlet contraction or expansion angles. The flow resistance curves indicate that the pressure loss coefficient K is primarily governed by the outlet geometry, while the influence of the inlet geometry is small. Blunt-ended stoppers induce a strong flow separation that leads to high K values, that remain relatively constant for the complete range of operation. This results in a good flow controllability and the advantage that these stoppers are less vulnerable for fouling and wear. In contrast, streamlined stoppers exhibit low K values that yet sharply increases at the onset of cavitation, and potentially lead to instabilities in valve throughput. The common geometry in the steel casting industry is somewhere in between these geometries, and may be improved based on the current findings.

The cavitation phenomena in the current study are governed by vaporous cavitation. Given the negligible vapor pressure in liquid steel, and the presence of dissolved gasses (i.e., N_2), vaporous cavitation is highly unlikely and gaseous cavitation is anticipated. Gaseous cavitation is not as destructive as vaporous cavitation, while gas bubbles will not implode but rather slowly dissolve. This will positively affect potential cavitation damage or wear to the SEN or stopper geometry. Yet, gaseous cavitation will still result in flow blockage and flow instabilities, similar to the flow resistance curves that are discussed in the present study.

Future research will also focus on the effect of non-soluble (i.e., Argon) gas injection on the flow control characteristics and the cavitation behavior, as this is commonly applied during continuous casting of steel. Again, we suspect this will strongly affect valve behavior. Further experiments should shed light how the injection location will affect the flow resistance curves and cavitation inception and dynamics.

CRediT authorship contribution statement

Willian Hogendoorn: Writing – review & editing, Writing – original draft, Supervision, Resources, Methodology, Investigation, Formal analysis, Conceptualization. **René Delfos:** Supervision, Resources, Methodology, Investigation, Formal analysis, Conceptualization. **Guus Tulen:** Writing – original draft, Visualization, Methodology, Investigation, Formal analysis, Conceptualization. **Dennis Kappert:** Writing – original draft, Visualization, Methodology, Investigation, Formal analysis, Conceptualization. **Stijn de Bruin:** Writing – original draft, Visualization, Methodology, Investigation, Formal analysis, Conceptualization. **Job van Essen:** Writing – original draft, Visualization, Methodology, Investigation, Formal analysis, Conceptualization. **Dirk van der Plas:** Supervision, Resources, Investigation, Formal analysis, Conceptualization.

Declaration of competing interest

The authors declare that they have no known competing financial interests or personal relationships that could have appeared to influence the work reported in this paper.

Appendix A. Supplementary data

Supplementary material related to this article can be found online at https://doi.org/10.1016/j.ijmultiphaseflow.2026.105753.

Data availability

Data will be made available on request.

References

Avila, K., Moxey, D., De Lozar, A., Avila, M., Barkley, D., Hof, B., 2011. The onset of turbulence in pipe flow. Science 333 (6039), 192–196.
Bai, H., Thomas, B.G., 2001a. Effects of clogging, argon injection, and continuous casting conditions on flow and air aspiration in submerged entry nozzles. Met. Mater. Trans. B 32, 707–722.
Bai, H., Thomas, B.G., 2001b. Turbulent flow of liquid steel and argon bubbles in slide-gate tundish nozzles: Part I. model development and validation. Met. Mater. Trans. B 32, 253–267.
Chaudhary, R., Lee, G.-G., Thomas, B.G., Cho, S.-M., Kim, S.-H., Kwon, O.-D., 2011. Effect of stopper-rod misalignment on fluid flow in continuous casting of steel. Met. Mater. Trans. B 42, 300–315.
Cui, Y., Cheng, B., Ding, Q., Li, X., Zhao, M., 2023. Study on cavitation bubble characteristics in centrifugal pump based on image recognition. Processes 11 (12), 3314.

Dauby, P.H., 2012. Continuous casting: make better steel and more of it!. Met. Res. Technol. 109 (2), 113–136.
Deo, B., Boom, R., 1993. Fundamentals of Steelmaking Metallurgy. Prentice Hall International.
Eames, I.W., Milazzo, A., Maidment, G.G., 2014. Modelling thermostatic expansion valves. Int. J. Refrig. 38, 189–197.
Fang, Q., Zhao, P., Zhang, H., Zhou, W.-h., Yu, G., Wang, J.-h., Ni, H.-w., 2024. Formation of free-surface vortex and vortex suppression by rotating stopper-rod at end of tundish casting. J. Iron Steel Res. Int. 1–13.
Ganesh, H., 2015. Bubbly shock propagation as a cause of sheet to cloud transition of partial cavitation and stationary cavitation bubbles forming on a delta wing vortex. Ph. D. Thesis.
Ganesh, H., Mäkiharju, S.A., Ceccio, S.L., 2016. Bubbly shock propagation as a mechanism for sheet-to-cloud transition of partial cavities. J. Fluid Mech. 802, 37–78.
Gawandalkar, U.U., Poelma, C., 2024. The characteristics of bubbly shock waves in a cavitating axisymmetric venturi via time-resolved X-ray densitometry. J. Fluid Mech. 988, A34.
Gluzman, I., Thomas, F.O., 2022. Image-based characterization of the bubbly shock wave generation and evolution in aviation fuel cavitation. Phys. Rev. Fluids 7 (8), 084305.
Guthrie, R.I., Isac, M.M., 2022. Continuous casting practices for steel: Past, present and future. Metals 12 (5), 862.
Hattori, S., Nimura, A., Yada, H., 2013. Effect of temperature on cavitation erosion of 9cr steel in liquid metal. Wear 303 (1–2), 269–275.
Idelchik, I.E., Steinberg, M., Martynenko, O.G., 1986. Handbook of Hydraulic Resistance, vol. 2, Hemisphere publishing corporation New York.
Jahangir, S., Hogendoorn, W., Poelma, C., 2018. Dynamics of partial cavitation in an axisymmetric converging-diverging nozzle. Int. J. Multiph. Flow 106, 34–45.
Javurek, M., Thumfart, M., Wincor, R., 2010. Investigations on flow pattern and pressure inside SEN below stopper rod. Steel Res. Int. 81 (8), 668–674.
Lee, T.L., Khong, J.C., Fezzaa, K., Mi, J.W., 2013. Ultrafast X-ray imaging and modelling of ultrasonic cavitations in liquid metal. In: Materials Science Forum, vol. 765, Trans Tech Publ, pp. 190–194.
Liu, R., Forman, B., Yin, H., Lee, Y., 2023. A new insight into the flow and pressure behavior of a stopper rod flow control system. Steel Res. Int. 94 (6), 2200626.
Liu, R., Thomas, B.G., Sengupta, J., Chung, S.D., Trinh, M., 2014. Measurements of molten steel surface velocity and effect of stopper-rod movement on transient multiphase fluid flow in continuous casting. ISIJ Int. 54 (10), 2314–2323.
Louhenkilpi, S., 2024. Continuous casting of steel. In: Treatise on Process Metallurgy. Elsevier, pp. 343–383.
Marschall, H., Mørch, K.A., Keller, A., Kjeldsen, M., 2003. Cavitation inception by almost spherical solid particles in water. Phys. Fluids 15 (2), 545–553.
Mørch, K.A., 2015. Cavitation inception from bubble nuclei. Interface Focus. 5 (5).
Olia, H., van der Plas, D., Thomas, B.G., 2023. Pressure distribution and flow rate behavior in continuous-casting stopper-rod systems: PFSR. Met. Mater. Trans. B 54 (6), 2985–3009.
van Oord, J., Peeters, T., Westendorp, A., Higson, S., Brockhoff, J., 2007. Transition of the flow pattern in the feeding system. In: 2nd International Conference of Simulation and Modelling of Metallurgical Processes in Steelmaking, Graz, Austria.
Siddiqui, M.I.H., Jha, P.K., 2015. Numerical simulation of flow-induced wall shear stresses in three different shapes of multi-strand steelmaking tundishes. Steel Res. Int. 86 (7), 799–807.
Thomas, B.G., 2018. Review on modeling and simulation of continuous casting. Steel Res. Int. 89 (1), 1700312.
Thumfart, M., Javurek, M., 2015. Low pressure effects in SEN-stopper region in continuous casting. Steel Res. Int. 86 (1), 25–32.
Timmel, K., Wondrak, T., Röder, M., Stefani, F., Eckert, S., Gerbeth, G., 2014. Use of cold liquid metal models for investigations of the fluid flow in the continuous casting process. Steel Res. Int. 85 (8), 1283–1290.
Tzanakis, I., Lebon, G., Eskin, D., Pericleous, K., 2015. Comparison of cavitation intensity in water and in molten aluminium using a high-temperature cavitometer. In: Journal of Physics: Conference Series. 656, (1), IOP Publishing, 012120.
Wondrak, T., Eckert, S., Gerbeth, G., Stefani, F., Timmel, K., Peyton, A.J., Terzija, N., Yin, W., 2014. Visualization of the flow in a mold of continuous casting by contactless inductive flow tomography and mutual inductance tomography. Steel Res. Int. 85 (8), 1266–1273.
Yuan, Q., Thomas, B.G., Vanka, S., 2004a. Study of transient flow and particle transport in continuous steel caster molds: Part I. Fluid flow. Met. Mater. Trans. B 35, 685–702.
Yuan, Q., Thomas, B.G., Vanka, S., 2004b. Study of transient flow and particle transport in continuous steel caster molds: Part II. Particle transport. Met. Mater. Trans. B 35, 703–714.
Zhang, L., Yang, S., Cai, K., Li, J., Wan, X., Thomas, B.G., 2007. Investigation of fluid flow and steel cleanliness in the continuous casting strand. Met. Mater. Trans. B 38 (1), 63–83.
Zhong, L., Li, B., Zhu, Y., Wang, R., Wang, W., Zhang, X., 2007. Fluid flow in a four-strand bloom continuous casting tundish with different flow modifiers. ISIJ Int. 47 (1), 88–94.